Mechanics of a Restrained Layer of Floating Oil above a Water Current

Jerome H. Milgram* and Robert J. Van Houten†
Massachusetts Institute of Technology, Cambridge, Mass.

This paper determines the relative importance of interfacial shear stress and dynamic pressure in determining the thickness distribution of a layer of floating oil contained by a barrier above a water current. This is done by use of an equation relating vertical location of the oil-water interface, dynamic pressure, and shear stress. The interfacial shape is measured experimentally. The dynamic pressure is determined by numerical solution of the potential flow problem for flow beneath the measured shape. The aforementioned equation then yields the shear stress distribution. The rear portion of restrained oil layers are found to be governed by shear stress as are the forward portions for low current speeds. At higher current speeds, both dynamic pressure and shear stress are important in determining the shape of the forward portions. Large friction coefficients are shown to be due to flow over a rough interface resulting from the generation of Kelvin-Helmholtz waves on the interface. The entrainment of oil droplets into the water flow is shown to be the result of breaking of the Kelvin-Helmholtz waves.

Nomenclature

c_f = friction coefficient
g = acceleration due to gravity
G = Green's function
L,ℓ = coordinate along a boundary
M,m = graph of oil-water interface
n = coordinate normal to a boundary
N = as superscript, non-dimensional quantity
o = as subscript, oil
p = dynamic pressure
q = oil thickness
t = time
T_{0-a} = tension of oil-air interface
T_{0-w} = tension of oil-water interface
T_{w-a} = freestream velocity
U_0 = freestream speed
V_T = velocity tangential to an interface
w = as subscript, water
(x,y) = Cartesian coordinates
(ξ,η) = Cartesian coordinates
γ = vortex sheet strength
Φ,ϕ = velocity potentials
ρ = density
τ = shear stress
θ = angle between a boundary and x-axis

I. Introduction

When a floating layer of oil is restrained by an oil barrier in the presence of a current in the water beneath the oil, questions arise about the nature of the flow in the vicinity of the oil-water interface and about the shape taken on by that interface. These questions have important practical considerations for the cleanup of oil spills, not only when a spill is trapped by a barrier in the presence of a current, but also for sweeping operations utilizing towed barriers in open waters when the current is a relative one which is generated by the motion of the towed barrier. In a current, the planform shape of a barrier is nearly that of a catenary (cf. Milgram[1]) with the oil driven against the apex region of the catenary by the current. The thickness of the oil pool generally increases with distance from the leading edge of the contained pool to the apex. For any given oil type and barrier depth, excessive current speed or pool length will result in the pool becoming thick enough in the vicinity of the barrier for the oil to escape beneath it. This is called drainage failure. Although the hydromechanical forces on the entire oil layer affect the oil thickness distribution, and therefore containment failure by drainage, the final step is the escape of oil from the contiguous pool in the immediate vicinity of the barrier. As a result, the speed limit above which drainage failure occurs can be substantially raised by increasing the barrier draft. For a fixed length of the layer of oil contained by a barrier, the speed limit for drainage failure is roughly proportional to the square root of the barrier draft as shown by Cross and Hoult,[2] among others.

There is another type of containment failure whose speed limit is nearly independent of barrier draft. At relatively low current speeds (about 10 cm/s), the oil-water interface is smooth and free of visible waves. As the speed is increased, the interface first becomes unstable, with small waves being generated; at larger speeds oil droplets are torn off the interface, with some of these droplets being carried beneath the barrier by the current. This is called entrainment failure. For most oil types, barrier lengths (about 300 m) and barrier drafts (about 1 m) appropriate for use in unprotected waters, entrainment failure occurs at a lower speed than does drainage failure, so that is entrainment which dictates the current speed limit for effective containment.

The entrainment failure problem has stimulated this study of the oil-water interfacial mechanics. Inasmuch as the salient features of the situation are retained in the two-dimensional problem, which is more straightforward for both theoretical and experimental studies, this simpler problem is considered here. Figure 1 is a sequence of sideview photographs of a restrained oil layer in a "two-dimensional" flume for various current speeds ranging from 15 to 46 cm/s. With reference to that figure, it can be seen that the oil-water interface is very smooth in a current of 15 cm/s. At 23 cm/s, a few waves on the interface have formed and a slightly bulbous region, called a headwave, is generated just behind the leading edge of the slick. These features are considerably more apparent at a

---

Received Nov. 11, 1977; revision received April 6, 1978. Copyright © 1978 Massachusetts Institute of Technology with release to the American Institute of Aeronautics and Astronautics, Inc., to publish in all forms.

Index categories:Sea Pollution and Containment Control; Jets, Wakes, and Viscid-Inviscid Flow Interactions; Hydrodynamics.

*Professor of Ocean Engineering.

†Assistant Professor of Ocean Engineering.

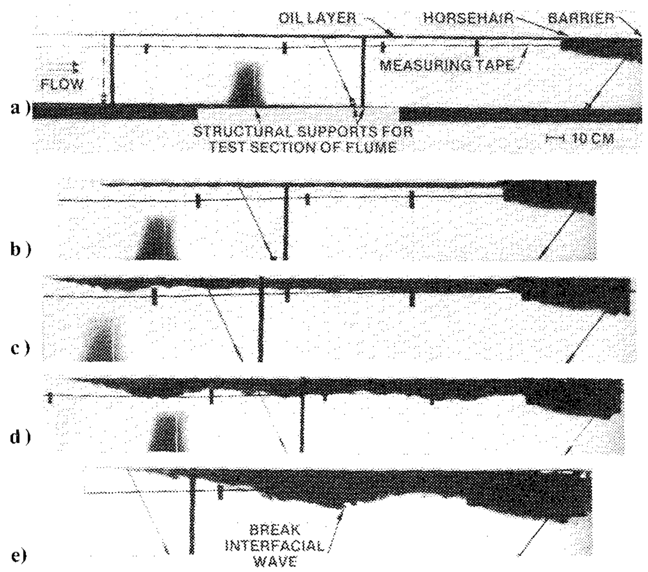

Fig. 1 Photographs of a restrained layer of dyed heavy mineral oil at various flow speeds: a) 15 cm/s, b) 23 cm/s, c) 30 cm/s, d) 38 cm/s, e) 46 cm/s.

current speed of 30 cm/s and they are further amplified at a speed of 38 cm/s. At a speed of 46 cm/s, the unsteady motion has become sufficiently violent for the interfacial waves to just begin to break and thereby generate droplets of oil which become entrained in the flowing water.

A number of studies have been carried out by other investigators on the problems related to a restrained oil layer over a moving current. Three of these, which were undertaken during almost identical times, were those of Wicks,[3] Cross and Hoult,[2] and Lindenmuth, Miller, and Hsu.[4] Although Wicks carried out experiments in a flume, he presented very little experimental data about the eqilibrium cross-sectional geometry of the oil layer or the entrainment of oil into the water. Rather, his paper concentrated on theoretical ideas suggested to him by his experimental observations. Wicks postulated that in the vicinity of the headwave, the problem is analogous to that of a gravity current "turned upside down." Gravity currents are those flows where a "wedge" of a heavier fluid flows under a lighter fluid such as a cold front intruding into warm air or salt water intruding into fresh water where a river or an estuary meets the sea. It has often been observed experimentally that a gravity current exhibits a headwave at its leading edge and an unstable region in the lee of that headwave. Analysis of such currents which have been carried out (cf. Von Karman[5] and Benjamin[6]) generally neglect shear forces at the interface between the two fluids. Wicks also neglected these forces in the vicinity of the headwave. The analysis of Benjamin[6] was actually carried out for a gas of negligible density, without a free surface above it, intruding into a layer of water bounded above a flat wall – essentially, a cavity flow. He showed that since a semi-infinite half body has no drag in potential flow, the unopposed hydrostatic driving force resulting from different water heights upstream and downstream leads to continuing acceleration of the water, in a reference frame affixed to the cavity. This result also applies if the cavity is "replaced" by a fluid in which the pressure is hydrostatic. Thus, such a steady potential flow is impossible. Benjamin predicted that the flow would become rotational as a result of wave breaking on the downstream side of the headwave.

Wicks observed instability and wave breaking on the lee side of the oil headwave and considered this to be analogous to Benjamin's results. However, there are two important differences between the oil layer problem and the idealized problem analyzed by Benjamin; namely, the existence of a free surface above the oil and a shear stress at the oil-water interface. These features remove the theoretical necessity for breaking of the headwave – a matter which Wicks did not consider.

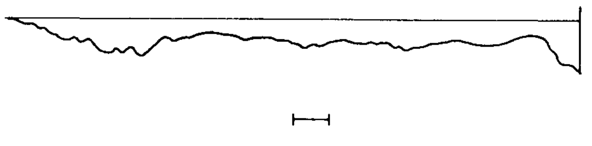

Fig. 2 Tracing of a photograph presented by Lindenmuth, Miller, and Hsu (1970). The test was done in a towing tank using no. 2 diesel oil with the boom towed at a speed of 40 cm/s.

Wicks suggested that, downstream of the headwave region, the dominant force causing a variation in oil layer thickness with spatial position is that of viscous shear at the interface, but he did not realize that this same shear force could be important in the headwave region as well. Interfacial waves which he observed in the downstream region were attributed to Kelvin-Helmholtz instabilities.

The study of Cross and Hoult[2] was based on experiments utilizing a barrier draft of only 3 cm. For this barrier draft, drainage failure occurred at a speed of about 15 cm/s and as a result the flow speeds they used were so slow that they never observed a headwave. This suggested their analysis wherein hydrostatic forces in the oil "wedge" were balanced by viscous shear forces of the water on the bottom of the oil pool. In particular, they showed that for a spatially constant shear stress, the depth of the oil would be proportional to the square root of the distance from the leading edge.

The work of Lindenmuth, Miller, and Hsu[4] was based on towing tank experiments wherein a barrier spanning the tank was towed at a fixed speed with oil in front of it. Figure 2 is a tracing of one of their photographs taken at a tow speed of 40 cm/s. The similarity to Fig. 1 is apparent. The only analysis given by Lindenmuth, et al. is identical to that of Cross and Hoult with the assumption of a spatially constant shear stress. The value of the skin friction coefficient was estimated as that value which resulted in a slick length equal to the observed slick length for the volume of oil used in the experiments. However, considering the profile shown in Fig. 2 as one whose height is proportional to the square root of distance from the leading edge is clearly unjustified.

Wilkinson[7] presented experimental and theoretical results for the shallow depth case in which the oil pool thickness was of the same order of magnitude as the water depth. In a similar manner to that of Wicks, Wilkinson considered a region in the vicinity of the headwave where viscous forces in the water could be neglected and a region further downstream where viscous forces and dynamic pressure forces related to the water being shallow were retained. These latter forces vanished in his analysis for water depths which were large in comparison to oil layer thickness. Although most of Wilkinson's work is related to shallow depth effects, he did present a photograph of an oil layer whose thickness was only about 1/10 of the water depth and which looked very much like the photographs and drawing presented here in Figs. 1 and 2.

An extensive experimental study of oil layers contained by a barrier above flowing water in a flume was reported by Hale, Norton, and Rodenberger.[8] Many of their results dealt with containment devices and the effects of waves and were therefore unrelated to our study. However, they did confirm that in a current much more droplet generation occurs in the vicinity of the headwave than elsewhere on the oil-water interface.

Leibovich[9] postulated that all the traveling waves which are found on the oil-water interface at speeds in excess of about 15 cm/s are Kelvin-Helmholtz waves whose amplitudes are limited by finite-amplitude effects similar to those analyzed by Drazin.[10] Leibovich further postulated that oil droplet formation leading to entrainment failure is the result of breaking of these Kelvin-Helmholtz waves. This hypothesis was in contradiction to that of Wicks and Wilkinson, who contended that droplet formation was due to the dissipative process described by Benjamin for cavity flows where viscous shear cannot equilibrate the hydrostatic forces. Although Drazin's analysis is based on current speeds only slightly in excess of the minimum speed needed to generate Kelvin-Helmholtz waves, it indicates that the equilibrated wave slope increases with increasing current speed. Leibovich showed that if wave breaking occurs for wave slopes on the order of unity, and if Drazin's theory holds for current speeds considerably in excess of the Kelvin-Helmholtz minimum speed, wave breaking will occur for the conditions in which Lindenmuth, et al. observed entrainment failure. Leibovich argued that the deepest portion of the headwave is often the deepest portion of the entire oil layer and this leads to a maximum in local water velocity which in turn results in the strongest Kelvin-Helmholtz instability being in the vicinity of the deepest portion of the headwave. He used this argument to explain why most droplet formation is observed on the lee side of the headwave.

Van Houten[11] observed that restrained oil slicks are slender, even in the region of the headwave. Using the force-equilibrium equation subsequently presented here, and expressing interfacial values of the flow variables in terms of their values at the undisturbed free surfaces, he posed a series of problems for flow quantities of zero, first, and second order with respect to the average interfacial slope and the density difference ratio $\Delta = (\rho_w - \rho_o)/\rho_w$. It was found that a necessary condition for slick slenderness was the dominance of friction forces everywhere along the slick, not just on the downstream portion.

The previous work described above raises an important question: What are the relative roles of the interfacial shear forces and the dynamic pressure forces in the water at the oil-water interface in determining the equilibrium thickness distribution of a restrained oil layer? A fundamental result for gravity currents derived by Von Karman[5] is that the included angle at the leading edge between the bottom and the interface must be 120 deg, thus indicating a 60-deg angle inside the gravity current between the bottom and the interface. If dynamic forces were dominant for the restrained oil layer problem, and if it be presumed that the hydrostatic pressure approximation is valid in the oil, a similar analysis indicates that the included angle at the leading edge between the water-air interface and the water-oil interface must be 120 deg. Although the water-air interface need not be horizontal, a straightforward analysis shows that it can deviate from the horizontal by only a few degrees. Therefore, if dynamic forces were dominant in the headwave region of a restrained oil layer, the included angle of the oil layer at the leading edge would have to be nearly 60 deg. Reference to Figs. 1 and 2 shows, however, that the included angle is about an order of magnitude smaller than 60 deg. This provides preliminary evidence that dynamic forces are not dominant in the headwave region, but complete evidence awaits the analysis which follows.

Much of our work was oriented toward a determination of the frictional and pressure forces on the oil layer. This was done by combining theory with experimental measurements. In the theory we assumed that the potential flow approximation for the flow in the water is accurate for predicting pressures in the water. With measurements of the mean oil layer thickness distribution, we have used Green's Theorem to calculate the flow in the water and the resulting pressure along the bottom of the oil layer. The calculated pressure and the measured oil thickness distribution are used in an equation we have derived which relates interfacial shape, pressure, and shear stress in order to determine the shear stress distribution. This then permits comparisons to be made and some definitive conclusions to be reached about the nature and relative effects of shear forces and pressure forces on the slick thickness distribution.

Our observations of the formation of oil droplets and of conditions leading to droplet formation are described in the following sections. From these observations, we are able to conclude that the droplets are generated by the breaking of Kelvin-Helmholtz waves, but we are not able to determine the quantitative details of the relative effects of forces of gravity, interfacial tension, dynamic pressure, and viscosity on the droplet generation process.

II. Theoretical Considerations

A. Flow in the Water

Consider water flowing from left to right under an oil layer as sketched in Fig. 3. The water is presumed to be infinitely deep and is bounded above by air for $x<0$ and by the restrained, floating oil layer for $x>0$. Under part of the water-air interface and beneath the oil, a boundary layer forms which is assumed to be thin enough for irrotational flow calculations to yield an accurate representation of the pressure along the boundaries.

The flow velocity is taken as the constant U_0 far upstream and far downstream. Thus, direct effects of the barrier on the water flow are neglected and far downstream the oil is "replaced" by a plane horizontal surface in the mathematical problem.

The vertical location of the upper boundary is called M, which is decomposed as

$$M(x,t) = m(x) + m^u(x,t) \tag{1}$$

where

$$m(x) = \overline{M(x,t)} \tag{2}$$

The overbar denotes the operation of time averaging, m is the steady component of the boundary position, and m^u is the time varying component caused by waves and turbulence resulting from instabilities in the flow. The velocity potential Φ is similarly decomposed as:

$$\Phi(x,y,t) = \phi(x,y) + \phi^u(x,y,t) \tag{3}$$

An integral equation for the velocity potential will be formulated by use of Green's Theorem and the Green's Function:

$$G = (1/2\pi)\ln r \tag{4}$$

where

$$r = [(x-\xi)^2 + (y-\eta)^2]^{1/2} \tag{5}$$

and (ξ,η) are "observation" points and (x,y) are "boundary" points. For this Green's Function, Green's Theorem is:

$$\Phi(\xi,\eta,t) = \oint \Phi(x,y,t)\frac{\partial G}{\partial n_{xy}}|\mathrm{d}L_{xy}| - \oint G\frac{\partial \Phi}{\partial n_{xy}}|\mathrm{d}L_{xy}| \tag{6}$$

where the path of integration is around all boundaries of the flow and $|\mathrm{d}L_{xy}|$ is the time varying differential element of arc length in (x,y) space. $\partial/\partial n_{xy}$ represents the derivative with respect to distance in the direction of the outward normal in (x,y) space. Expanding ϕ^u in powers of interfacial motion amplitude, writing the Green's Functions and integrals in Eq. (6) along $y=M$ in terms of those along $y=m$ by use of Taylor series expansions, and taking the time average and dropping terms of order 2 and higher in motion amplitude yields the

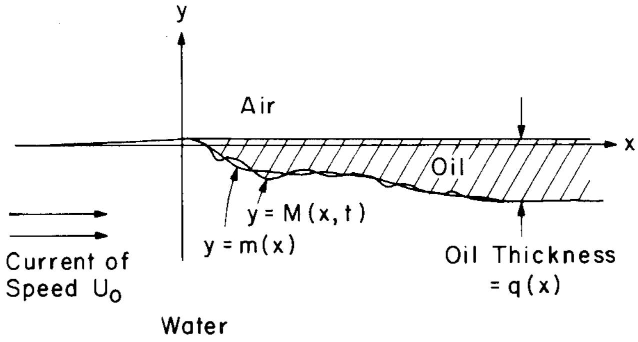

Fig. 3 Geometry for the oil layer thickness distribution problem.

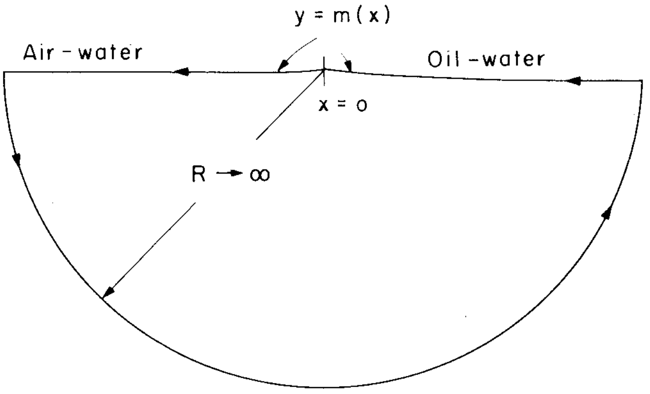

Fig. 4 Integration path used for the application of Green's Theorem.

following equation for the steady component of the motion:

$$\phi(\xi,\eta)=\oint \phi(x,y)\frac{\partial G}{\partial n_{xy}}\,|\mathrm{d}\ell_{xy}|-\oint G\frac{\partial \phi}{\partial n_{xy}}\,|\mathrm{d}\ell_{xy}| \qquad (7)$$

where $|\mathrm{d}\ell_{xy}|$ for the upper boundary is along $m(x)$.

The path of integration to be used in solving Eq. (7) is shown in Fig. 4. Contributions to the integrals from the semi-circular part of the path can be readily evaluated and, in the limit as the radius of the semi-circle becomes large, the contribution to the first integral becomes $U_0\xi/4$, the second becomes $-U_0\xi/4$. The integrand of the second integral vanishes on the upper boundary. Thus, taking the directional derivative of Eq. (7) along m "just below" the upper boundary yields the integral equation for the tangential velocity along this boundary, after integrating by parts, as:

$$V_T(\xi,\eta)=\frac{U_0}{2}\cos\theta+\int_{m_{xy}} V_T(x,y)\frac{\partial G}{\partial n_{xy}}\,|\mathrm{d}\ell_{xy}| \qquad (8)$$

where V_T is the tangential velocity, taken as positive from left to right in Fig. 3, $\int_{m_{xy}}$ denotes the integral along the curve m, and θ is the angle between m and the horizontal axis. This can be viewed as representing the flow as that induced by a vortex sheet of spatially varying strength V_T along the upper boundary. The dynamic pressure p in the water of density ρ_w along the oil-water interface is given by Bernoulli's equation as:

$$p=(\rho_w/2)(U_0{}^2-V_T{}^2) \qquad (9)$$

Equation (8) for V_T will be solved numerically in Sec. IV for each mean free surface shape $m(x)$ measured in the experiments. It should be noted that Eq. (8) is insensitive to changes in length scale, thus permitting the subsequent calculations to be done using the natural unit U^2/g as the unit of length. The non-dimensional pressure $\bar{p}$ is defined by:

$$\bar{p}=p/\rho_w U_0{}^2 \qquad (10)$$

and it is related to V_T by Bernoulli's equation as:

$$\bar{p}=\tfrac{1}{2}[1-(V_T/U_0)^2] \qquad (11)$$

B. Force Equilibria in the Oil

The measurements of Hale, Norton, and Rodenberger,[8] as well as measurements we have made, show that throughout most of the thickness of the oil layer, velocities in the oil are about one order of magnitude smaller than those in the water beneath the interfacial boundary layer. Therefore, oil dynamic pressures and oil momentum fluxes can be neglected and the pressure in the oil can be taken as hydrostatic. Using these facts, a force-balance differential equation for the oil will be derived. The mean forces on the differential length of the oil layer are shown in Fig. 5. These are pressure forces on the vertical faces and forces on the lower face due to steady pressure, viscous shear stress, and the Reynolds stress associated with the unsteady components of oil depth and pressure. In a way which is analogous to the shear stress on a rough wall, the shear and Reynolds stresses are lumped into the mean shear stress τ, expressed in terms of the friction coefficient c_f by:

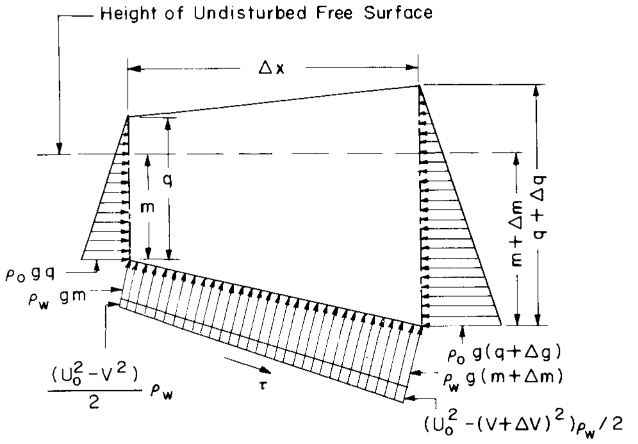

Fig. 5 Forces acting on a differential element of length of the oil layer.

$$\tau(x)=\tfrac{1}{2}\rho_w U_0{}^2 c_f(x) \qquad (12)$$

Balancing horizontal forces on the differential element of length of the oil layer and letting its length approach zero gives:

$$\rho_w gm\frac{\mathrm{d}m}{\mathrm{d}x}+p\frac{\mathrm{d}m}{\mathrm{d}x}+\frac{\rho_w}{2}c_f U_0{}^2=\rho_o gq\frac{\mathrm{d}q}{\mathrm{d}x} \qquad (13)$$

where q is the mean thickness of the oil, g is the acceleration due to gravity, and ρ_o is the density of the oil. The interfacial pressure is taken as equal in the oil and the water, and the pressure at the air interface is taken as constant (zero), since the curvatures of the mean interfacial shapes are small enough to make the related mean pressure discontinuities caused by the effects of surface tensions to be entirely negligible.

For continuity of pressure at the oil-water interface:

$$q=(\rho_w gm+p)/\rho_o g \qquad (14)$$

Substituting Eq. (14) for q in Eq. (13) then gives the differential equation for force equilibria in the oil layer as:

$$\left(gm+\frac{p}{\rho_w}\right)\left(g\Delta\frac{\mathrm{d}m}{\mathrm{d}x}+\frac{1}{\rho_w}\frac{\mathrm{d}p}{\mathrm{d}x}\right)=\frac{g}{2}(1-\Delta)c_f U_0{}^2 \qquad (15)$$

where

$$\Delta=(\rho_w-\rho_o)/\rho_w \tag{16}$$

Non-dimensional lengths $\tilde m$ and $\tilde x$ are defined by:

$$\tilde m=gm/U^2 \tag{17}$$

$$\tilde x=gx/U^2 \tag{18}$$

Then, Eq. (15) can be written in non-dimensional form as:

$$(\tilde m+\tilde p)\left(\Delta\frac{\mathrm{d}\tilde m}{\mathrm{d}\tilde x}+\frac{\mathrm{d}\tilde p}{\mathrm{d}\tilde x}\right)=\tfrac{1}{2}(1-\Delta)c_f \tag{19}$$

This is the basic equation that relates the shape of the oil-water interface to the forces on the interference generated by the dynamic pressure in the mean water flow and by the friction related to flow over the rough interface.

III. Experiments

A. Apparatus and Procedures

The experiments were carried out in the Precision Flume of the MIT Department of Ocean Engineering. An isometric transparent cut-away view of this device is shown in Fig. 6. The main reason for construction of the flume was to perform the experiments described here. The glass-walled test section of the flume is 6.25 m long, with cross-sectional dimensions of 61 cm in height and 46 cm in width. Apart from the downstream adjustable tilting weir and the sump tank beneath it, the remainder of the flume is a "wind tunnel type" circuit. Such a circuit was used to minimize freestream turbulence in the test section whose rms velocities were found to be less than 0.5% of the freestream speed. The height of the liquid in the test section and the flow speed are controlled by adjustments of the speed of the motor driving the flume and the height of the adjustable tilting weir. The sump tank serves two purposes: one is that of a free surface basin of low mean speed to allow entrained air and oil to rise to the surface, and the other is to serve as a place from which to collect oil after the completion of a test. More details about the flume are given by Milgram and Van Houten.[12]

To conduct a test, an oil barrier as shown in Fig. 6 was installed in the test section. Normal operating fluid depth in the test section was 53 cm, and the barrier extended to a depth of 17.5 cm below the free surface. Such a barrier alone is inadequate for containing oil in a flume test. The reason for this is that the vorticity from the flume sidewall boundary layers accumulates in the corners between the sidewalls and the barrier, thus forming a strong vortex in each corner with the cores of these vortices going down and beneath the barrier. These vortices can draw oil down beneath the barrier giving a form of drainage failure peculiar to a flume test. To overcome this difficulty, a layer of rubberized horsehair was installed on the upstream side of the barrier. This horsehair spanned the width of the flume and had a thickness equal to the height of the barrier. The length of the section of horsehair was approximately 60 cm. The rubberized horsehair served to diffuse and dissipate the concentrated vorticity entering it from the sidewall boundary layers so that no strong vortices in the vicinity of the floating oil were formed.

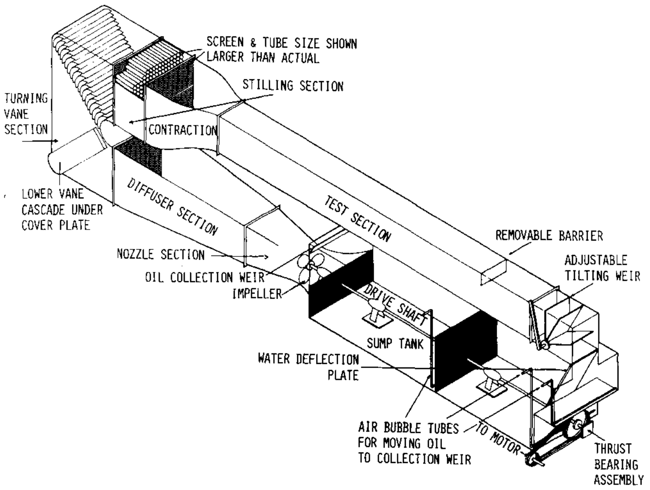

Fig. 6 Isometric transparent cut-away view of the flume. Supporting structural elements are not shown.

After the flume was brought up to the desired speed, oil was layered onto the water in the test section and then allowed to come to equilibrium. Attainment of an equilibrium mean geometry was sometimes observed to take as long as several minutes. During this time, the thickness would come to equilibrium by means of a sequence of long slow moving waves moving back and forth in the oil layer. The speed of these waves is limited to $\sqrt{\Delta gq}$ so that when the oil layer is relatively thin several minutes are required for a wave to pass through the slick several times. It is because of these waves and the fact that an equilibrium geometry is attained by means of them that towing tank tests for experiments of this type cannot be used unless the tank is extremely long.

A priori calibrations for flume test section flow speed as a function of drive motor rpm and weir height were used for approximate settings of test section flow speed. Then for each experiment, the speed was measured more precisely by measuring the time for a neutrally buoyant particle to move a known distance. Speed adjustments were made as necessary by adjustments in weir height and drive motor speed.

Interfacial shapes were measured by two methods. One was that of direct measurements of the heights of the water-air, water-oil, and oil-air interfaces at the glass sidewall of the test section. Since the interfacial heights were not constant, but varying due to interfacial waves, as well as small and slow variations of flume speed, an average measurement had to be made by observing the height at a fixed value of x over a period of time and averaging "by eye."

The second method of measurement was from photographs taken from the side of the flume which showed the interfacial locations at one instant. In this case, each observed shape was the sum of the mean shape and the unsteady wave motion on the interface. To obtain the mean shape from the photographs, the interfacial shape was graphically smoothed before offsets were taken from the photograph. Figure 7 shows a tracing of the oil layer in one of the photographs, as well as the graphically smoothed shape made from the photograph, from which mean oil layer thickness measurements were taken.

B. Oil Types and Flow Speeds

Table 1 shows the physical properties of all the oil types used in these experiments. For each oil type, experiments were carried out over a range of flow speeds varying from 16 cm/s to an upper speed limit restricted by excessive drainage or entrainment loss of the oil past the barrier.

The first group of tests were conducted with light mineral oil and with heavy mineral oil, with interfacial locations determined by direct measurement. Subsequent tests were all conducted with measurements made from photographs. The second group of tests included a repeat of the heavy mineral

Fig. 7 a) A tracing of Fig. 1d and b) the corresponding graphically smoothed shape.

Table 1 Oil properties

Oil type	Δ	Kinematic viscosity (centiStokes)	Air-oil tension (dyn/cm)	Oil-water tension (dyn/cm)
Heavy mineral	0.120	125.36	33.7	37.0
Heavy mineral with 0.1% Zonyl A surfactant	0.120	125.36	33.0	1.6
Light mineral	0.140	12.24	28.6	30.8
Arzew crude	0.196	4.52	27.6	29.4
No. 2 diesel	0.163	3.61	30.5	23.7
No. 2 diesel with 0.1% Zonyl A surfactant	0.163	3.61	29.2	1.5

oil tests, and tests with an Algerian crude oil known as Arzew. For the heavy mineral oil, although drainage failure began at a current speed of 38 cm/s, the rapidity with which photographs could be taken permitted interface shapes to be measured up to a speed of 45.7 cm/s. In the case of the Arzew crude, drainage failure did not occur unless the speed exceeded 50 cm/s. We were surprised to observe that there was only very little droplet formation and entrainment loss of the oil in all of the conditions described above, whereas other investigators reported substantial entrainment failure at speeds below 30 cm/s. Inasmuch as the reported entrainment failure was usually for diesel oil (cf. Lindenmuth, et al.[4]), we conducted a series of tests with diesel oil at speeds between 16 and 50 cm/s. Droplet formation and entrainment loss were observed at speeds above 29 cm/s with the diesel oil.

Finally, tests were conducted using diesel oil and then heavy mineral oil, each containing 0.1% of a surfactant known as Zonyl A. This material, made and sold by E. I. Dupont de Nemours and Co., Inc., lowers the interfacial tension between the oil and the water to approximately 1.5 dyn/cm for the oils and concentrations used in our tests. In the case of the diesel oil with surfactant, the tests were made immediately after the tests of the diesel oil alone without changing the water in the flume. The amount of oil entrained in the water by the time of the tests of diesel oil with surfactant made the water so cloudy that accurate measurements of the interface shape could not be made. However, we were able to observe the generation and entrainment of droplets. Fresh, clean water was used for the tests of mineral oil with surfactant.

C. Experimental Observations

Initially, we attempted to determine the shear stress on the oil from measurements of the velocity distribution within the oil layer. However, instead of finding the expected result of the lower portion of the oil moving downstream and the upper portion moving upstream everywhere, we found that the oil moved very slowly in the form of circulation cells with vertical axes. For example, one region of the oil-air interface would be moving downstream while another region was moving upstream. Thus, we were not able to directly determine skin friction coefficients from measurements of the oil flow. Hale, Norton, and Rodenberger[8] reported similar difficulties in obtaining friction estimates from direct measurements of the oil surface velocity coupled with measurements of the water velocity within the boundary layer.

The mean motion of the oil was very slow through the oil layer and in most cases was at least an order of magnitude slower than the freestream water speed. From the slowness of this motion, we could conclude that the pressure distribution within the oil could be approximated as hydrostatic pressure. This does not apply to the time-varying component of the motion associated with the traveling interfacial waves.

At very slow water speeds, the oil-water interface was smooth. When the speed was increased to about 20 cm/s, waves on the interface were observed. We questioned whether these waves were Kelvin-Helmholtz waves or the result of the fluctuations in Tollmien-Schlichting waves. They appear to be Kelvin-Helmholtz waves for the following three reasons:

1) The characteristics of Kelvin-Helmholtz waves depend on fluid densities, interfacial tensions, and flow speed, but not on downstream location. For a given oil type and flow speed, the waves we observed had constant phase speed and wavelength as they moved downstream, thus behaving as Kelvin-Helmholtz waves. On the other hand, Tollmien-Schlichting waves would be expected to become longer and move more slowly as they moved downstream as a result of the increasing Reynolds number and boundary layer thickness with downstream position.

2) As the flow speed was slowly increased, the waves first appeared near the leading edge of the oil slick, as would be expected for Kelvin-Helmholtz waves because the shear layer in the water is stronger there than it is further downstream. Tollmien-Schlichting waves would be expected to appear downstream first, owing to the larger Reynolds number based on slick length for downstream regions than for upstream regions.

3) At the higher flow speeds when the interface is quite rough, starting a short distance downstream from the region where the waves begin, the boundary layer must become turbulent and cease to support Tollmien-Schlichting waves having any regularity. However, we observed interfacial waves possessing some regularities over almost the entire slick, although their amplitudes were substantially diminished far downstream. This indicates that they were not Tollmien-Schlichting waves.

The waves did not appear right at the leading edge, but rather appeared a short distance aft of the leading edge. Very near the leading edge the oil is very thin and it has been shown by Leibovich[9] that thin oil layers are more stable with respect to Kelvin-Helmholtz waves than thick oil layers. This result is due to the fact that the oil-air tension has a stablizing influence when the layer is thin, but has less influence when the layer is thicker.

Significant entrainment of droplets into the water was not observed to occur over the range of speeds of our experiments for either type of pure mineral oil, or for the Arzew crude oil. Droplet entrainment did occur with diesel oil for speeds in excess of 29 cm/s.

The only measured physical property affected by the addition of 0.1% Zonyl A surfactant to either the diesel oil or the heavy mineral oil was the lowering of the oil-water interfacial tension to approximately 1.5 dyn/cm in each case. With the diesel oil containing surfactant, oil droplet entrainment was observed to occur at all speeds in excess of 23 cm/s. With the mineral oil containing surfactant, droplets were formed at all speeds in excess of 30 cm/s. Figure 8 shows a close-up photograph of the headwave region of mineral oil with surfactant at a flow speed of 34 cm/s.

In most instances, the form of the leading edge of the oil layer was not that of a straight line across the flume, but rather a U-shaped line when viewed from above, with regions near the side of the flume being upstream of regions near the center of the flume. The deviation from a straight line was usually less than ±5 cm. However, in the case of the diesel oil, the deviation from a straight line was sometimes as much as ±12 cm. For reasons which we do not yet understand, the leading edge of the layer of mineral oil containing the surfactant was almost completely straight with deviations from the straight line usually being less than ±2 cm. In graphically smoothing the measured interface shapes for subsequent data analysis, the smoothed leading edge position was taken approximately midway between the most upstream and most downstream portions of the leading edge.

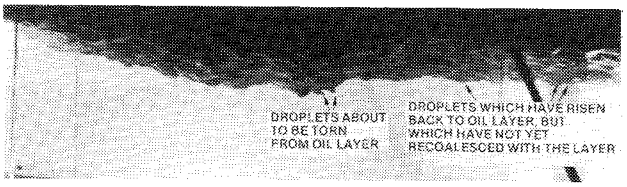

Fig. 8 Close-up of headwave region of mineral oil containing surfactant at a flow speed of 34 cm/s.

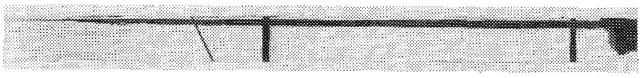

Fig. 9 Photograph of layer of mineral oil with surfactant at a flow speed of 23 cm/s, showing thin tongue of oil upstream from headwave region.

Whenever the surface flow in a channel is completely blocked by a surface-piercing barrier, surface contaminants accumulate into a thin layer, often of submicron thickness, ahead of the barrier. The upstream end of this "surface film region" is marked by a visable ridge on the water surface called the "demarcation line" by McCutchen[13] and also known as Thoreau-Reynolds ridge (McDowell and McCutchen[14]). In our experiments a surface film formed upstream of the oil layer as evidenced by a demarcation line. This film typically grew in length at a rate of about 1 cm/s until it reached a length between 25 and 150 cm, at which point its length remained constant. A boundary layer forms in the water flow beneath the film with the horizontal shear stress of the water flow on the film balanced by the surface tension gradient in the film. Thus, the water boundary layer has a non-zero thickness at the leading edge of the bulk region of the oil layer.

In the case of the surfactant-treated mineral oil, a thin tongue of oil was observed to exist in the leading edge region with the length of this thin region being considerably more than was the case for the same conditions and the oil without the surfactant. For example, at a speed of 23 cm/s, the length of the thin region with the surfactant-treated oil was approximately 36 cm. A photograph of this is shown in Fig. 9. This should be compared with Fig. 1 showing a photograph of the same type of oil, but without surfactant at the same flow speed. The thin tongue is not the "surface film region" which is very much thinner, but we believe the tongue is related to the film region in a way described in Sec. V.

IV. Data Analysis

The purpose of our data analysis was to determine the relative effects of pressure forces and frictional forces in determining the oil layer thickness distribution. The first step in the analysis was to use the measured interfacial shapes to determine the "potential flow" tangential velocity in the water by means of numerical solutions to Eq. (8). Details of the method of numerical solution are given in the Appendix. The measured interfacial shape and the interfacial pressure distribution calculated from Eq. (11) were used in Eq. (19) to determine the distribution of skin friction.

In order to compare the relative effects of friction and pressure in determining the interfacial shape, it is useful to calculate the interfacial shape which the calculated skin friction distribution would yield in the absence of dynamic pressures. This relationship is established by setting the dynamic pressure and its horizontal derivative to zero in Eq. (19) and then solving for $\tilde{m}$. Calling this solution $\tilde{m}_f$, we obtain:

$$\tilde{m}_f(\tilde{x}) = \left[\frac{1-\Delta}{\Delta}\int_0^{\tilde{x}} c_f(\tilde{x}')\,\mathrm{d}x'\right]^{1/2} \tag{20}$$

For each oil layer thickness distribution which we analyzed, we calculated $c_f(x)$ and $\tilde{m}_f(x)$. Figures 10 through 15 show graphs of the smoothed measured interfacial shapes $\tilde{m}$, the calculated pressure distribution $\tilde{p}$, the calculated friction distribution c_f, and the calculated shapes $\tilde{m}_f$ that would be obtained in the presence of the calculated friction but without dynamic pressure.

V. Discussion and Conclusions

Due to the presence of the relatively short traveling interfacial waves, measurements of the mean thickness distribution had to be made with time averaging for direct measurements and with graphical smoothing for measurements taken from photographs. The degree of accuracy and repeatability of the mean thickness measurements is best understood by comparing the results of the two methods.

Figures 10(b) and 11(a) are for identical conditions, with the interface shape measured directly for 10(b) and by smoothed measurements from a photograph for 11(a). The measurements were taken from entirely separate experiments and the results are very similar. Figures 10(c) and 11(b) are for supposedly identical conditions at a flow speed of 28 cm/s. Figure 10(c) is from direct measurements and Fig. 11(b) is from measurements of a photograph. Some differences in the results can be observed. However, the results in 10(c) lie approximately between those for 11(b) and those for 11(c), which are for a flow speed of 30 cm/s. Therefore, the differences between Figs. 10(c) and 11(b) can be attributed to an error in speed measurement of about 1 cm/s. Speed measurement errors of this order were entirely possible with our method of speed measurement. Thus, the two methods of measurement of the shape of the oil-water interface do lead to similar results.

An examination of the calculated interfacial friction distributions in Figs. 10 through 15 show that most fall into one of two types, which we refer to as Type I and Type II. Type I is that exhibited by Figs. 10(a,b), 11(a), 12(a,b,c), 14(a), and 15(a). It is characterized by a friction coefficient that is small near the leading edge and which builds up to a maximum lying in the range of 0.013 to 0.073 in the vicinity of the region of maximum curvature of the headwave, this region being that of a local maximum in oil thickness in cases where the headwave is actually deeper than regions just aft of it. The maximum friction coefficient increases with increasing flow speed for each oil type. Behind the region of maximum friction coefficient, the friction diminishes to values in the range of 0.004 to 0.012 over the remainder of the oil layer. Presumably, the friction coefficients would continue to decrease to smaller values if the layers were longer.

Type II is that exhibited in Figs. 10(c), 11(c,d,e), 13(c), 14(c,d), and 15(b,c). It is characterized by small values near the leading edge and it rises to a local maximum as distance aft of the leading edge is increased. Then it drops rapidly, achieving its minimum value, which may be either positive or negative, just forward of the region of maximum headwave depth. Next, it rises rapidly and achieves a local maximum just aft of the region of maximum headwave depth. It falls to a small negative local minimum value near the first local maximum in interface depth aft of the headwave. The amount of change that the friction coefficient undergoes in the abovementioned variations increases with flow speed. Values in the range from −0.16 to +0.33 were observed. Downstream of the last mentioned minimum in the friction coefficient it rises to positive values smaller than the large maximum on the leeward side of the headwave and usually retains small positive values over the remainder of the layer, but oscillates between small positive and negative values when the interfacial shape is oscillatory. The friction coefficients for Figs. 11(b), 13(a,b), and 14(b) appear to be midway between Type I and Type II. Type I friction coefficients occur

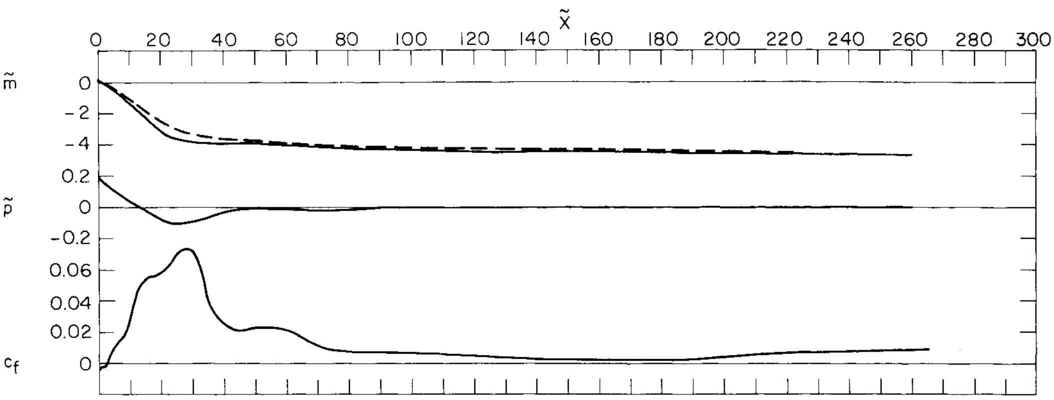

a) water speed = 17 cm/s

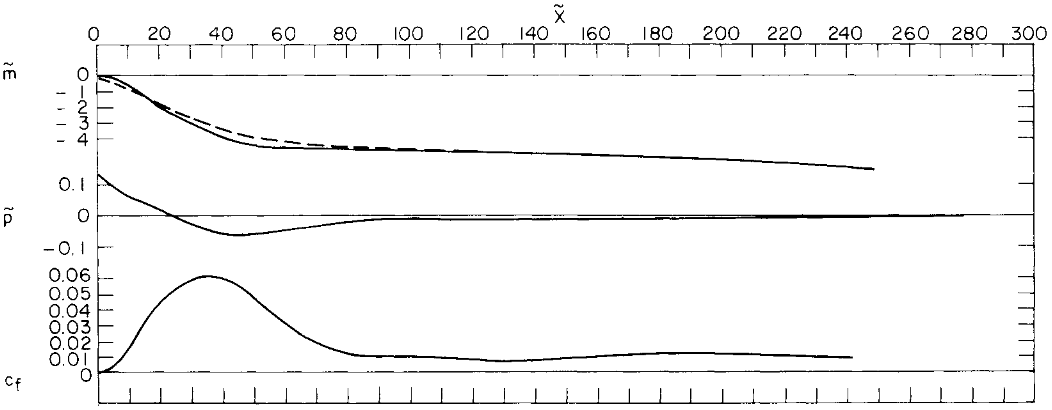

b) water speed = 23 cm/s

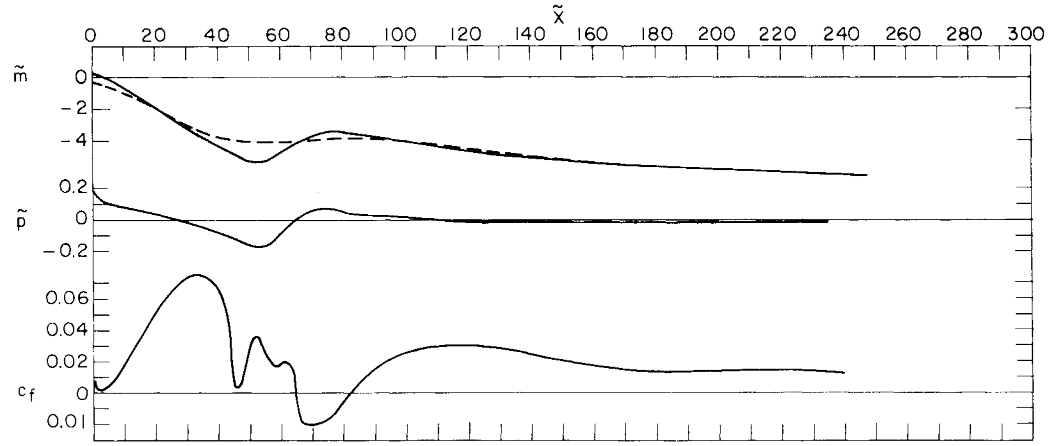

c) water speed = 29 cm/s

Fig. 10 Smoothed, measured interfacial shapes ($\tilde{m}$), shapes due to friction alone ($\tilde{m}_f$), calculated pressures ($\tilde{p}$), and calculated friction coefficients (c_f), for heavy mineral oil (data measured directly). $\tilde{m}$ is shown by solid lines; $\tilde{m}_f$ is shown by dashed lines.

for cases having small interfacial waves and for such cases the predominant influence on the boundary layer in the water is expected to be the pressure gradient. Because of the existence of the surface film region, the boundary layer has developed some thickness at the leading edge of the oil. Just downstream from the leading edge the boundary layer thickness probably decreases because of the favorable pressure gradient in this region. Further downstream – for example, at $\tilde{x} = 28$ in Fig. 10(a) – the pressure gradient turns unfavorable and just downstream from this location the friction coefficient starts decreasing with increasing downstream position.

The dependence of the maximum in friction coefficient in the vicinity of the headwave on flow speed is undoubtedly due to "surface roughness" of the Kelvin-Helmholtz waves which are largest in the vicinity of the headwave and whose amplitudes increase with increasing flow speeds.

Type II friction coefficients occur for cases where the Kelvin-Helmholtz waves are large and very steep, such as can be seen in Fig. 1(d), which corresponds to the results shown in Fig. 11(d). The order of magnitude of the wave slope is unity. Although some aspects of the Type II friction distributions can be attributed to the pressure gradients, it is clear that the overall situation is much more complicated than for Type I distributions. Where the friction coefficient attains its largest values, there is no doubt that this is due to local time-varying flow separation behind the deepest parts of the Kelvin-Helmholtz waves.

For all the oil layer thickness distributions that were

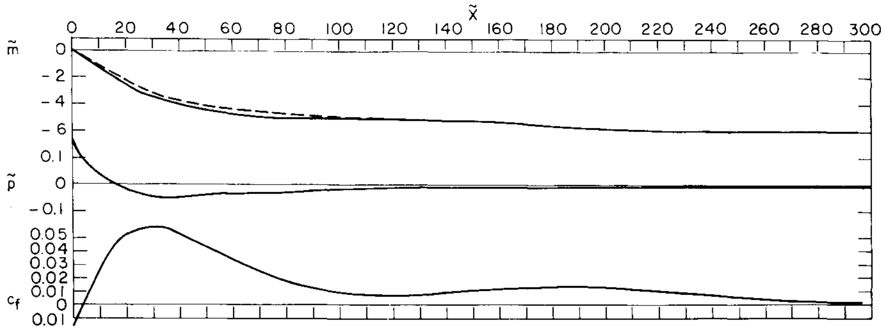

a) water speed = 23 cm/s

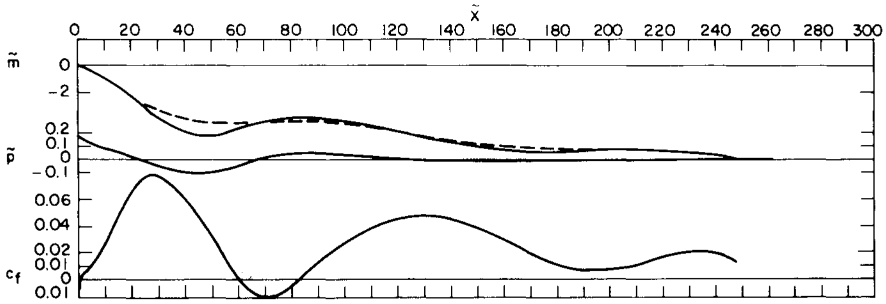

b) water speed = 29 cm/s

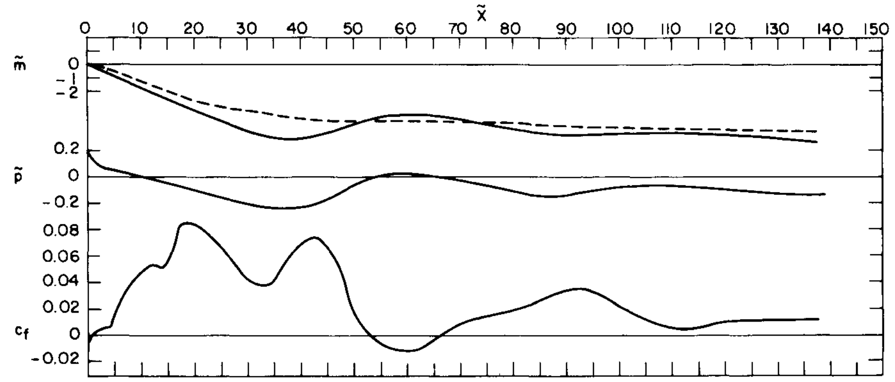

c) water speed = 30 cm/s

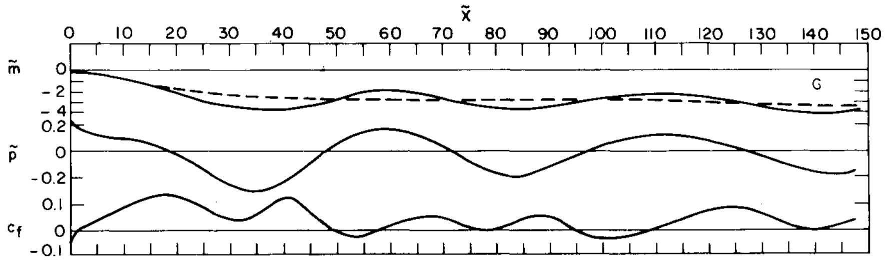

d) water speed = 38 cm/s

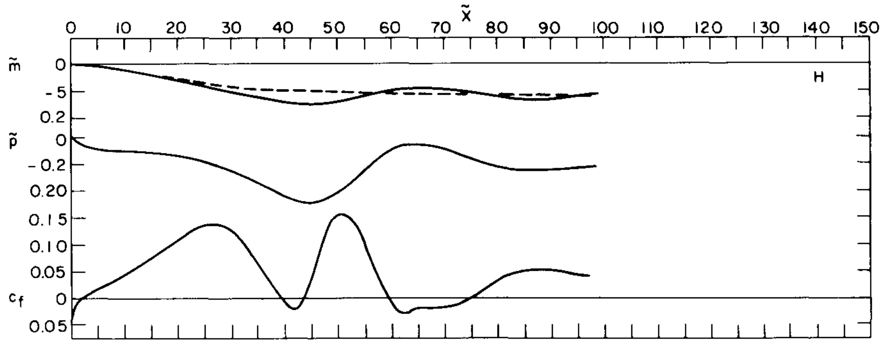

e) water speed = 46 cm/s

Fig. 11 Smoothed, measured interfacial shapes ($\tilde{m}$), shapes due to friction alone ($\tilde{m}_f$), calculated pressures ($\tilde{p}$), and calculated friction coefficients (c_f), for heavy mineral oil (data from photograph). $\tilde{m}$ is shown by solid lines; $\tilde{m}_f$ is shown by dashed lines.

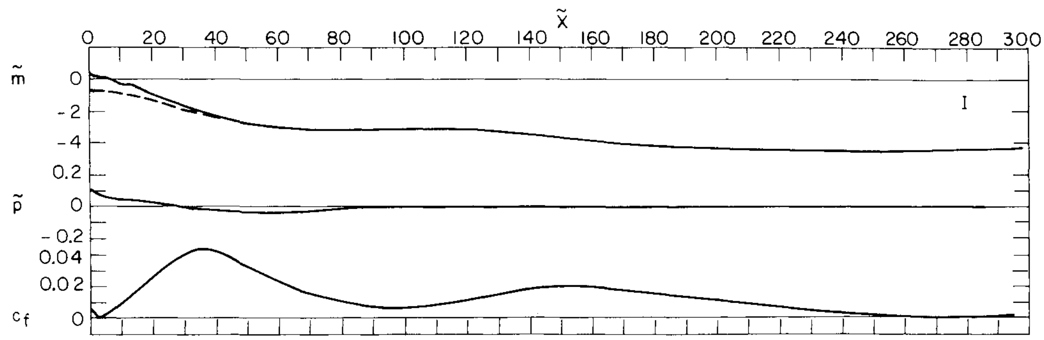

a) water speed = 18 cm/s

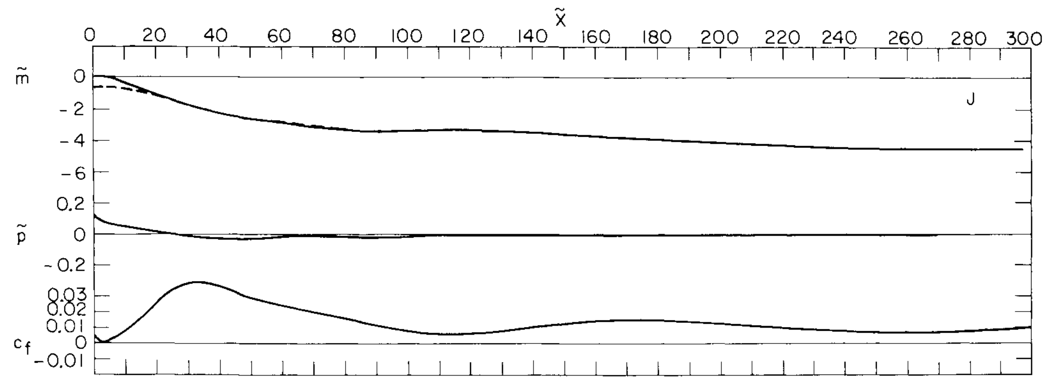

b) water speed = 23 cm/s

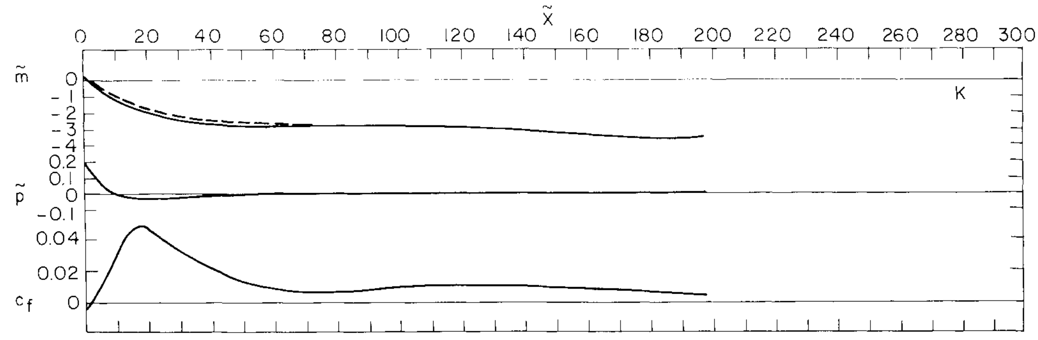

c) water speed = 29 cm/s

Fig. 12 Smoothed, measured interfacial shapes ($\tilde{m}$), shapes due to friction alone ($\tilde{m}_f$), calculated pressures ($\tilde{p}$), and calculated friction coefficients (c_f), for light mineral oil (data measured directly). $\tilde{m}$ is shown by solid lines; $\tilde{m}_f$ is shown by dashed lines.

measured, the portion of the layer thickness that can be attributed to friction alone is a significant portion of the total thickness over the entire extent of the oil layer. Over the rearward portion of the oil layer, the friction is the completely dominating factor in generating the layer thickness distribution. Therefore, the assumption that the friction was all important in determining the geometry of the rear portion of the oil layer by several previous investigators is justified. However, their assumption that friction is unimportant over the forward portion of the layer is ill-founded.

The generation of the oil droplets is related to the breaking of the Kelvin-Helmholtz waves as shown in the photographs of Figs. 1 and 8. The calculated results shown in Fig. 15(c) are for the same conditions as Fig. 8, for which $U_0 = 34$ cm/s. It can be seen that the region of droplet generation which is on the leeward side of the headwave is not only that of highest water velocity as evidenced by the low pressure, but also the region of maximum friction coefficient. Droplet formation was also observed on the leeward side of the headwave for the conditions of Fig. 15(b). For this region, $\tilde{p} = 0.14$, which indicates that the local water speed in this region is 34 cm/s from Eq. (11). This is the same local speed as exists for the downstream regions of the oil layer shown in Figs. 8 and 15(c), but these regions do not exhibit breaking waves or droplet generation. Thus, the droplet generation phenomenon is more complicated than that proposed by Leibovich,[9] which was that entrainment occurs with any specific oil wherever a certain critical current speed is exceeded in the flow beneath the oil, independent of the portion of the oil layer at which the required velocity occurs. The amplitude of the Kelvin-Helmholtz waves, which lead to droplet entrainment when they become large enough to break, depends not only on the water speed below the boundary layer in the water, but also on the boundary layer thickness. When the layer is thick, changes in interface shape lead to smaller pressure changes than when the layer is thin. Droplet formation is seen to be maximized by high water speeds and a thin boundary layer which is evidenced by a high friction coefficient. Downstream, where the boundary layer has been slowed and thickened by its prior passage over the rough surface, the Kelvin-Helmholtz wave amplitude is reduced, as is droplet formation.

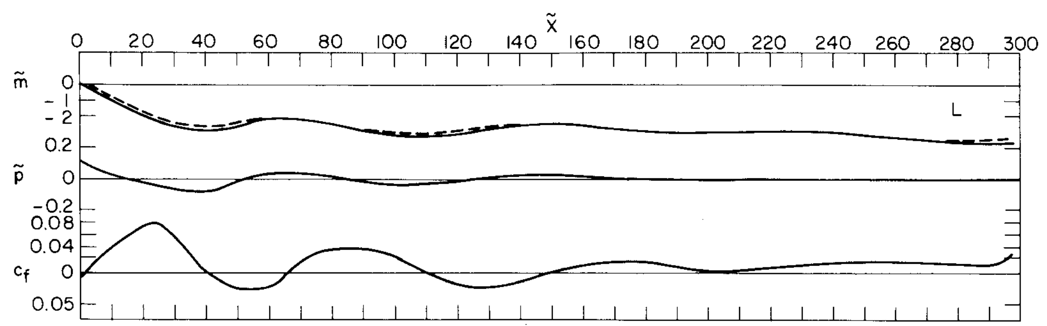

a) water speed = 29 cm/s

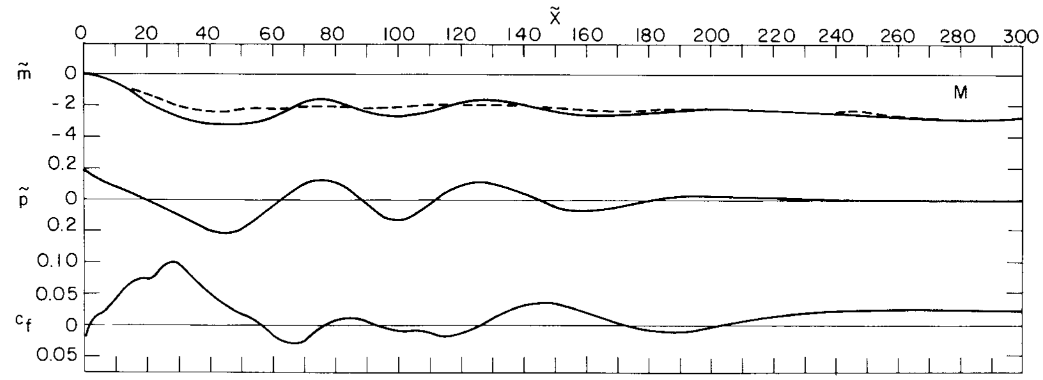

b) water speed = 38 cm/s

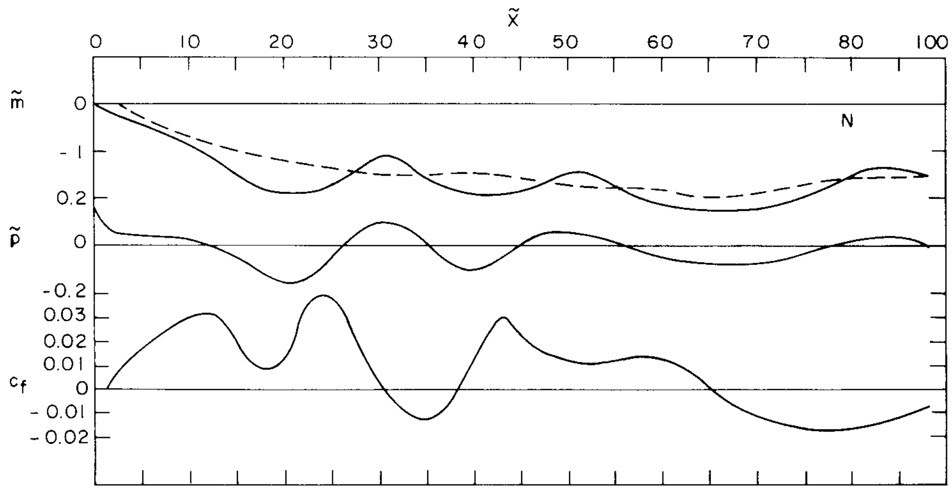

c) water speed = 46 cm/s

Fig. 13 Smoothed, measured interfacial shapes ($\tilde{m}$), shapes due to friction alone ($\tilde{m}_f$), calculated pressures ($\tilde{p}$), and calculated friction coefficients (c_f), for Arzew crude oil (data from photograph). $\tilde{m}$ is shown by solid lines; $\tilde{m}_f$ is shown by dashed lines.

The most unstable wavelength for classical Kelvin-Helmholtz waves is given by (cf. Lamb[15] or Leibovich[9]):

$$\lambda_{cr} = 2\pi \left[\frac{T_{o-w}}{\rho_w g \Delta} \right]^{1/2} \tag{21}$$

provided that the oil layer depth q is large enough to meet the depth requirement $\tanh(2\pi q/\lambda_{cr}) \simeq 1$. T_{o-w} is the interfacial tension on the oil-water interface. For the conditions of Figs. 8 and 15(c), $\lambda_{cr} = 4.3$ cm. Photographs of layers of that oil are shown in Fig. 1. Over most of the lengths of the oil layers the depth requirement is met. However, most of the observed waves in these figures have lengths in the range of 10 to 25 cm and it is certainly waves in this length range that break and lead to droplet entrainment. Evidently the relatively large damping of the very short waves prevents them from growing large enough to break.

Figure 16 is a close-up of the headwave of a diesel oil layer at a flow speed of 46 cm/s. For this oil, $\lambda_{cr} = 2.4$ cm. Since the kinematic viscosity of the diesel oil is less than 3% of that of the heavy mineral oil, the short waves undergo less damping in the diesel oil and as a result waves with wavelengths of the order of λ_{cr} are observed in the diesel oil in Fig. 11, whereas such waves are not observed in the mineral oil. Thus, it appears that viscosity of the oil plays a role in determining the critical speed for droplet entrainment through its effect on the Kelvin-Helmholtz waves.

A comparison of interfacial shapes and friction distributions for the heavy mineral oil (Figs. 10 and 11) with those for the same oil containing surfactant (Fig. 15) shows

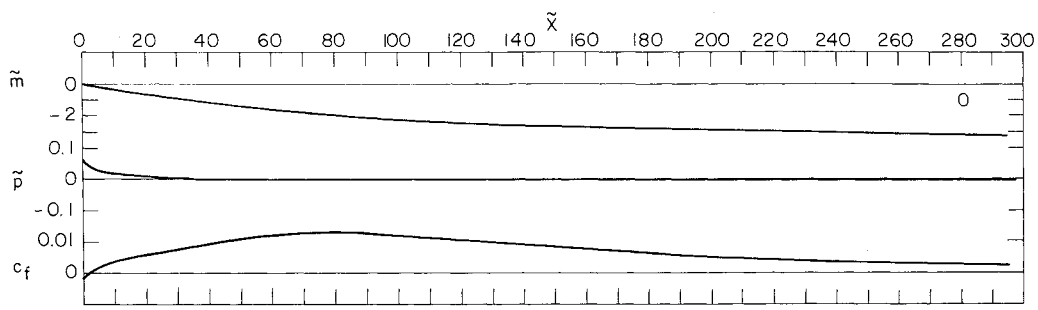

a) water speed = 23 cm/s (the dotted curve is coincident with the solid curve)

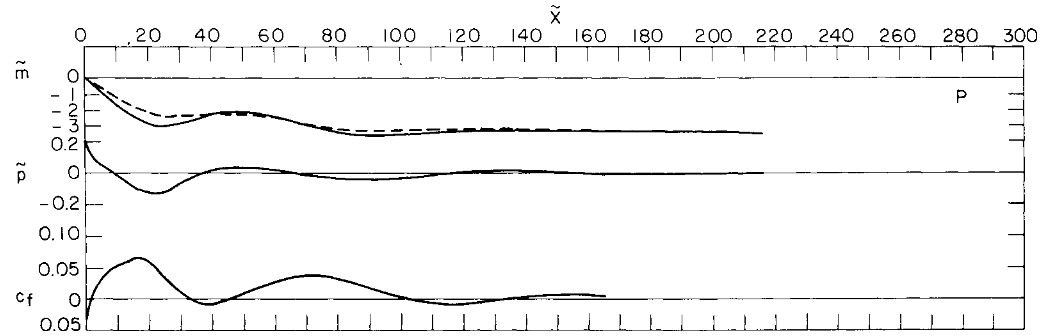

b) water speed = 29 cm/s

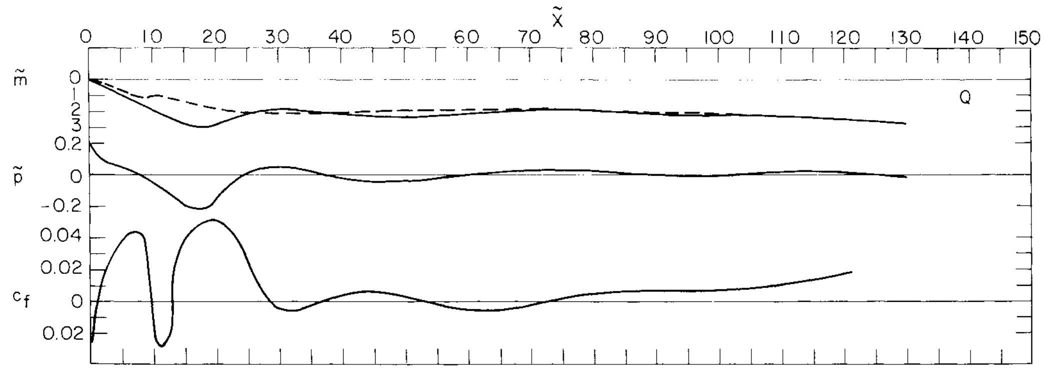

c) water speed = 38 cm/s

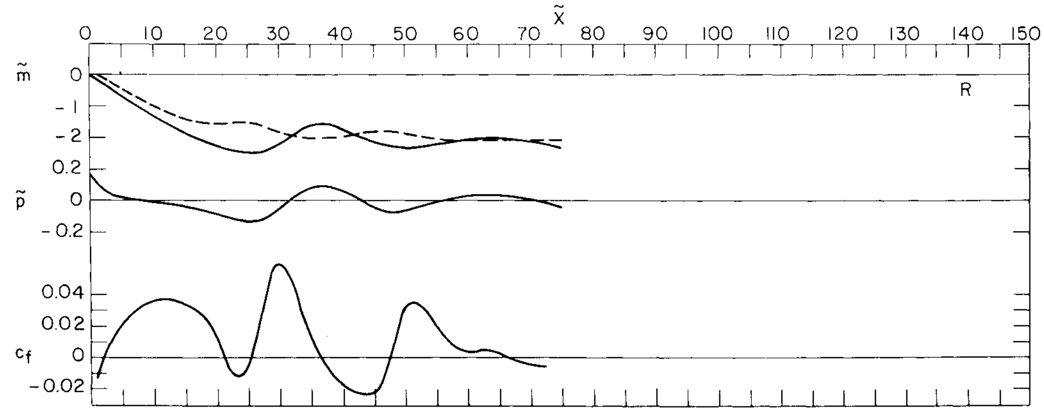

d) water speed = 46 cm/s

Fig. 14 Smoothed, measured interfacial shapes ($\tilde{m}$), shapes due to friction alone ($\tilde{m}_f$), calculated pressures ($\tilde{p}$), and calculated friction coefficients (c_f), for no. 2 diesel oil (data from photograph). $\tilde{m}$ is shown by solid lines; $\tilde{m}_f$ is shown by dashed lines.

that the enormous decrease in oil-water interfacial tension from 37 to 1.5 dyn/cm has relatively little effect on these quantities. At a speed of 23 cm/s [Figs. 10(b), 11(a), and 15(a)], the main effects of the surfactant are related to the leading-edge tongue.

In the presence of surfactant-treated mineral oil, the net spreading pressure is 38 dyn/cm, based on an oil-air tension of 72 dyn/cm, whereas in the absence of surfactant the net spreading pressure is 1 dyn/cm. The spreading pressure is given by:

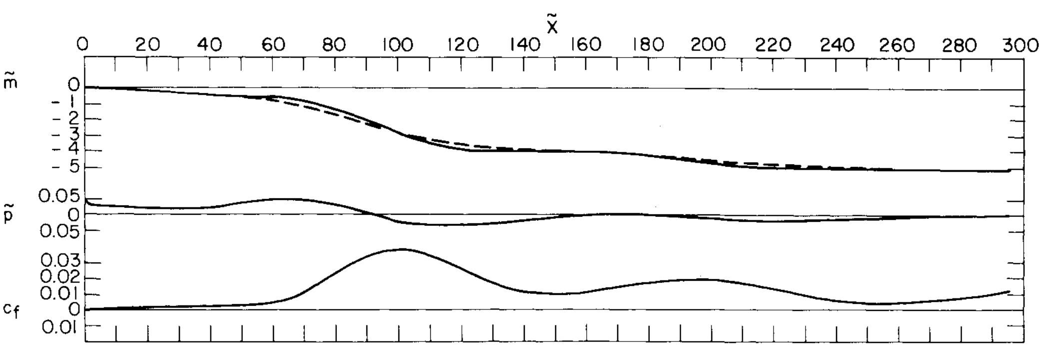

a) water speed = 23 cm/s

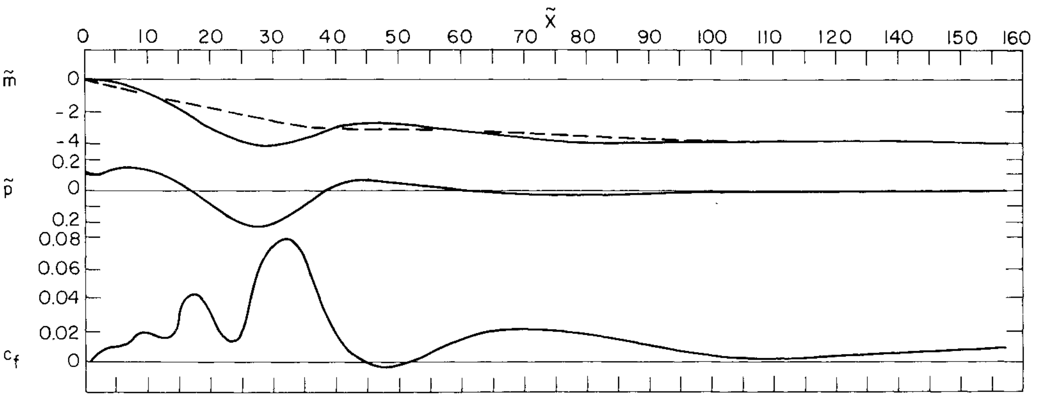

b) water speed = 30 cm/s

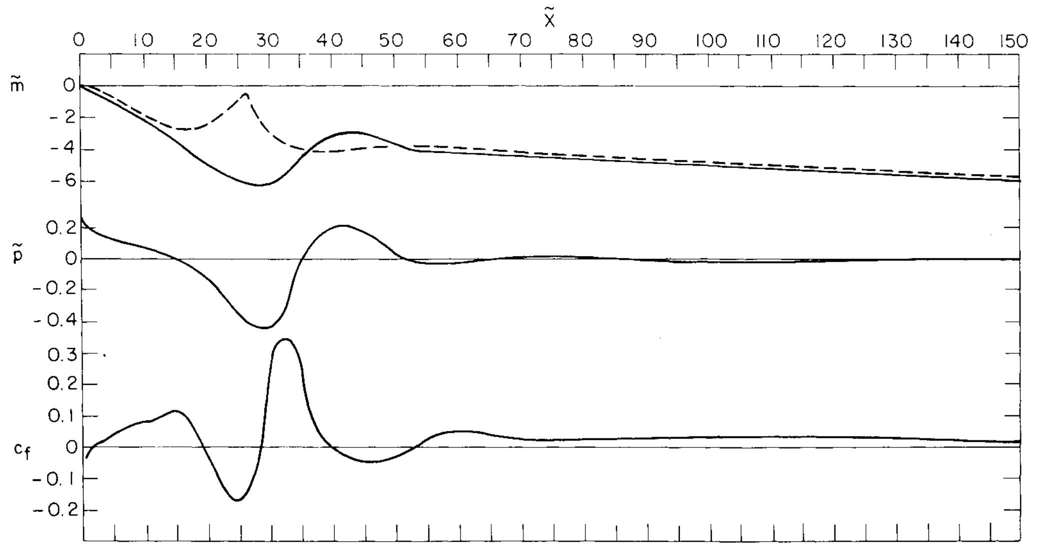

c) water speed = 34 cm/s

Fig. 15 Smoothed, measured interfacial shapes ($\tilde{m}$), shapes due to friction alone ($\tilde{m}_f$), calculated pressures ($\tilde{p}$), and calculated friction coefficients (c_f), for heavy mineral oil with .1% Zonyl A surfactant (data from photograph). $\tilde{m}$ is shown by solid lines; $\tilde{m}_f$ is shown by dashed lines.

$$S = T_{w-a} - T_{o-w} - T_{o-a} \tag{22}$$

Unless the surface contamination in the case of oil without surfactant has a spreading pressure of at least 38 dyn/cm, the surface film will be longer with the surfactant-treated oil. This would lead to a thicker boundary layer in the water and reduced shear stress on the oil at the leading edge of the bulk oil region, which would result in a decreased interfacial slope. We offer this as one possible explanation for the tongue, but we hasten to point out that evidence for it is not conclusive. The additional thickening of the boundary layer as the water flows beneath the tongue usually results in the maximum friction coefficient being slightly lower for oil with surfactant than for the pure oil. At a speed of 31 cm/s [Figs. 11(c) and 15(b)], results are nearly identical. At a speed of 34 cm/s for the case of oil with surfactant [Fig. 15(c)], the general features are similar to what would be expected at this speed for pure oil, based on an average of Fig. 11(c) for 31 cm/s and Fig. 11(d) for 38 cm/s. A specific feature that is different is that the peak friction coefficient for the oil with surfactant is 0.47. This is considerably larger than 0.18, which is the average of the friction peaks in Figs. 11(c) and 11(d). This isolated

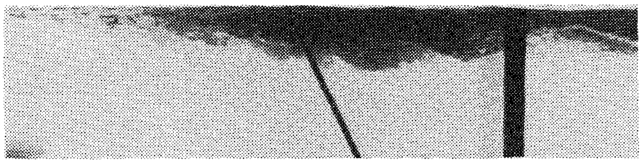

Fig. 16 Headwave region of a diesel oil layer in a current of 46 cm/s.

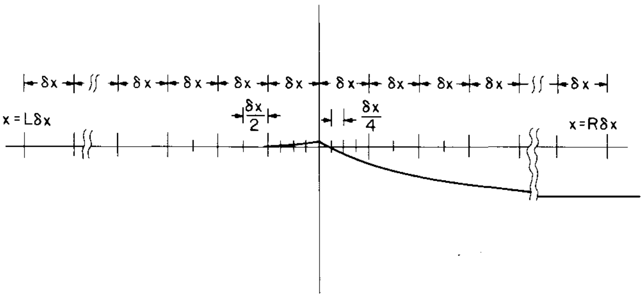

Fig. 17 Partitioning of the x-axis for the numerical solution.

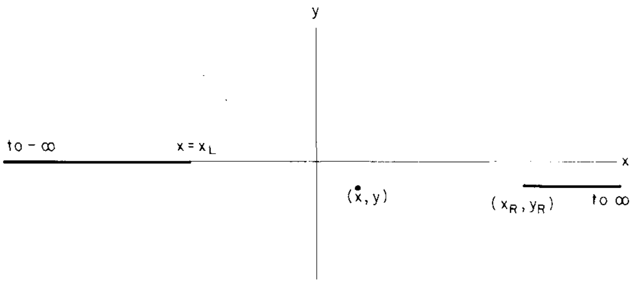

Fig. 18 Geometry for the calculation of the velocity at (x, y) induced by the semi-infinite vortex sheets. The sheets are shown by heavy lines and have strengths U_0.

feature is the most notable difference between results for oil with and without surfactant. It is due to the fact that the interfacial waves are just beginning to break for the oil with surfactant.

One is led to inquire why such a large decrease in interfacial tension has such a small effect on oil layer geometry. For theoretical Kelvin-Helmholtz waves satisfying the depth requirement given above, the critical flow speed for instability is proportional to $(T_{o-w})^{1/4}$. Also, as interfacial tension is reduced, all unstable wavelengths become more unstable, and more wavelengths become unstable. Why were these features not observed by their effect on the shear stress in our experiments? The answer lies in the effect of viscosity, which results in damping of the shortest waves as described above. The ratio of gravitional forces to interfacial tension forces in Kelvin-Helmholtz waves is $\rho_w g \Delta \lambda^2 / 4\pi^2 T_{o-w}$. For the theoretically most unstable waves, this ratio is exactly unity. However, for the longer waves that were observed, the ratio greatly exceeds unity. For example, for $\lambda = 15$ cm in pure mineral oil, the ratio is 12, and with surfactant in the oil the ratio is 294. Thus, the observed waves were dominated by gravity: it is for this reason that they were altered only slightly by a large change in interfacial tension. The tension does affect the conditions required for the waves to break and generate droplets; either as a result of small changes in the wave features, or by its direct effect on the breaking process.

Appendix: Method of Numerical Calculation of Tangential Velocity at the Oil-Water Interface

The integral equation, Eq. (8), for the tangential water velocity V_T at the oil-water interface expresses the velocity as that induced by a vortex sheet of strength $\gamma(x) = V_T$ along the mean interfacial boundary $m(x)$ superimposed on a horizontal flow of speed $U_0/2$.

The first step leading to a numerical solution is to partition the x-axis into divisions that are short enough so that $m(x)$ can be well approximated by a continuous function $m_a(x)$ that is linear over each division, and $\gamma(x)$ can be approximated by a function $\gamma_a(x)$ which is constant over each division. A basic length interval δx is chosen, whose size varies from $10U^2/g$ for the longest oil layers of our tests to $3U^2/g$ for the shortest oil layers. L of these length intervals are considered to the left of $x = 0$ and R are considered to the right as shown in Fig. 17. The interfacial shape $m(x)$ was considered to be horizontal for $x < -L\delta x$ and for $x > R\delta x$. Since velocity and interfacial shape variations are greatest near $x = 0$, the first basic length interval on each side of $x = 0$ is subdivided into four intervals of length $\delta x/4$, and the next two basic intervals on each side of $x = 0$ are each divided into two intervals of length $\delta x/2$ as shown in Fig. 17. Thus, the x-axis is divided into $(L + R + 10)$ intervals of finite length and two semi-infinite intervals. The finite intervals are labeled by the index j; $1 \leq j \leq (L + R + 10)$. The left-most interval is labeled $j = 1$, and so forth.

Far to the right and far to the left the tangential velocity is U_0, so that the vortex strength is set to U_0 over each of the semi-infinite intervals. Over the span of the finite length intervals, $\gamma_a(x)$ consists of the $(L + R + 10)$ values, γ_j, corresponding to the values of $\gamma_a(x)$ in each interval. The γ_j's represent the solution to the problem and are to be determined. The approximating integral equation is:

$$\gamma_a(\xi) = \frac{U_0}{2}\cos\theta + \int_{m_a} \gamma_a(x) \frac{\partial G}{\partial n_{xy}} |d\ell_{xy}| \qquad \text{(A1)}$$

Since there are $(L + R + 10)$ values, namely the γ_j's, that are unknown, Eq. (A1) can be satisfied at only $(L + R + 10)$ discrete points which are chosen here as the midpoints of the $(L + R + 10)$ intervals. The midpoints, which we call x_j, are special points because only at the midpoint of an interval is the velocity induced by the vortex strength over that interval independent of any linear variation in this vortex strength. Thus, by choosing the midpoints as the co-location points, the accuracy of the procedure is nearly equal to that of one in which the approximating vortex strength is continuous and piecewise linear. The only reduction in accuracy from that procedure which we encounter is our neglect of the effect of the linear variation in vortex strength in one interval on the velocity induced in another interval, an effect which is extremely small for the interfacial slopes we measured and interval sizes we have chosen. The values of $m_a(x)$ at $x = x_j$ are called m_j.

At the $(L + R + 10)$ values of x_j, Eq. (A1) can be written as:

$$\gamma_j = \frac{U_0}{2}\cos\theta_j + A_j + \sum_{k=1}^{L+R+10} B_{jk}\gamma_k \qquad \text{(A2)}$$

where θ_m is the interface angle at x_j, A_j is the tangential velocity induced at x_j by the two semi-infinite vortex sheets of strength U_0, and B_{jk} is the tangential velocity induced at x_j by an element of vortex sheet of unit strength over the kth interval. Once the measured interfacial shape and the A_j's and the B_j's are known, Eq. (A2) is just a set of $L + R + 10$ linear algebraic equations for $L + R + 10$ unknowns. Solving these numerically solves the problem.

The geometry for determining the velocity induced by the semi-infinite vortex sheets is shown in Fig. 18. The complex velocity w_E, where $w_E = u_E - iv_E$, induced at an arbitrary point z, where $z = x + iy$, is given by:

$$w_E(z) = -\frac{iU_0}{2\pi}\left[\int_{-\infty}^{x_L} \frac{d\beta}{z - \beta} + \int_{x_R}^{\infty} \frac{d\beta}{z - (\beta + iy_R)}\right] \qquad \text{(A3)}$$

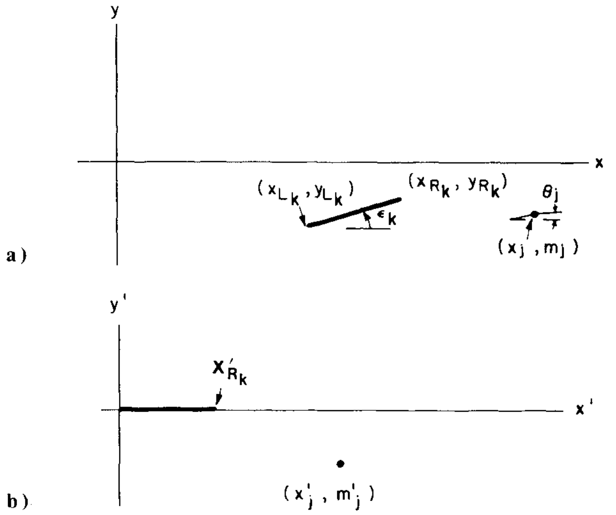

Fig. 19 Geometry for the calculation of B_{jk}. The vortex sheet represented by the heavy line is of unit strength. a) Shows the geometry in (x, y) coordinates. b) Shows the geometry after use of the coordinate transformation given by Eq. (A6).

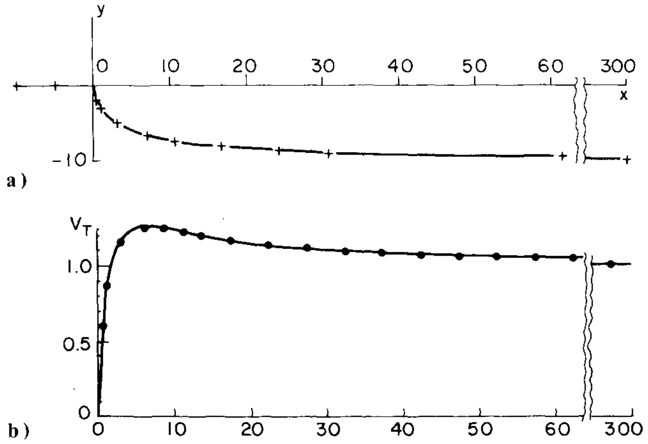

Fig. 20 Shape and tangential velocity distribution for stagnation streamline of a "source in a stream." a) Shape. Solid line is shape given by Eq. (A12). Crosses mark points used as input data to test procedure and computer program. b) Tangential velocity distributions. Solid line is theoretical velocity given by Eq. (A13). Dots are numerical results from computer program using our analysis procedure.

Evaluating this at $z_j = x_j + im_j$ gives

$$w_E(z_j) = \frac{iU_0}{2\pi}\ln\left[\frac{x_j - x_L + im_j}{x_R - x_j + i(y_R - m_j)}\right] \tag{A4}$$

Then A_j is found from

$$A_j = u_E(z_j)\cos\theta_j + v_E(z_j)\sin\theta_j \tag{A5}$$

The problem for determining B_{jk} is shown in Fig. 19. This problem is reduced to the simpler problem shown in the figure by the following coordinate transformation.

$$\begin{bmatrix} x' \\ y' \end{bmatrix} = \begin{bmatrix} \cos\epsilon_k & \sin\epsilon_k \\ -\sin\epsilon_k & \cos\epsilon_k \end{bmatrix} \begin{bmatrix} x - x_{L_k} \\ y - y_{L_k} \end{bmatrix} \tag{A6}$$

where

$$\epsilon_k = \tan \frac{y_{R_k} - y_{L_k}}{x_{R_k} - x_{L_k}} \tag{A7}$$

The complex velocity w'_{jk}, where $w'_{jk} = u'_{jk} - iv'_{jk}$ at the point z'_j due to the vortex sheet element of unit strength $(0 \le x' \le x'_{R_k})$, is given by:

$$w'_{jk} = -\frac{i}{2\pi}\int_0^{x'_{R_k}} \frac{d\beta}{z'_j - \beta} = \frac{i}{2\pi}\ln\left(\frac{x'_{R_k} - z'_j}{-z'_j}\right) \tag{A8}$$

u_{jk} and v_{jk} for the problem of Fig. 19(a) are then given by the transformation:

$$\begin{bmatrix} u_{jk} \\ v_{jk} \end{bmatrix} = \begin{bmatrix} \cos\epsilon_k & -\sin\epsilon_k \\ \sin\epsilon_k & \cos\epsilon_k \end{bmatrix} \begin{bmatrix} u'_{jk} \\ v'_{jk} \end{bmatrix} \tag{A9}$$

so B_{jk} is then given by

$$B_{jk} = u_{jk}\cos\theta + v_{jk}\sin\theta \tag{A10}$$

For $k = j$, B_{jj} is obtained by taking the limit as z approaches the midpoint of the interval from below, which results in:

$$B_{jj} = 1/2 \tag{A11}$$

Experimental measurements were made of the oil-water interface, leading edge angle, and of m at 8 to 11 points on the smoothed oil-water interface. In addition, for the data obtained by direct measurement, m was measured at three or four points along the water-air interface, and for these cases the angle of the water-air interface at $x = 0$ was measured. The water-air interface was very nearly flat, so it was taken as exactly flat for data measured from photographs on all of which the water-air interfacial displacements were too small to measure. The interfacial shapes were numerically fit with "spline curves," which are local cubics having continuous displacements, slopes, and curvatures except at $x = 0$, where we required only displacement to be continuous and slopes on each side to equal the specified values. These curves passed through the measured data points and had the measured angles at $x = 0$. Values of m at the end and midpoints of each interval were then calculated from the spline curves; the A_j's and B_{jk}'s were then calculated as described above and the set of linear algebraic equations (A2) were then solved numerically to obtain the tangential velocity at the midpoint of each interval.

In order to check the total computer program, a test was made using the points from the dividing streamline shape for a "source in a stream" as the input data for the interference shape. The stream speed was specified as 1.0, the source was located at $x = 10/\pi$, and the source strength used was $10/\pi$, so the "nose" was at $x = 0$. Thus, the theoretical interfacial shape is given by:

$$y = 0 \quad , \; x < 0$$

$$\frac{\pi}{\pi x - 10} = -\frac{1}{y}\tan\frac{\pi y}{10} \; , \; x > 0 \tag{A12}$$

and the theoretical tangential velocity is:

$$V_T = \left[1 + \frac{20\pi x}{(\pi x - 10)^2 + \pi^2 y^2} - \frac{100}{(\pi x - 10)^2 + \pi^2 y^2}\right]^{1/2} \tag{A13}$$

Since the "spline curve" cannot have infinite slope, the initial angle of the "oil-water" side of the streamline with respect to the x-axis was specified as 83 deg. The results of theoretical and computed interfacial velocity are shown in Fig. 20.

Acknowledgments

This work was supported in part by the National Science Foundation under Grant Number ENG72-03943 A04, and in part by the M.I.T. Sea Grant Program through Grant

Number 04-6-158-44081 of the Office of Sea Grant, National Oceanic and Atmospheric Administration. The Arzew crude oil was contributed by the Shell Development Corporation.

References

[1] Milgram, J. H., "Forces and Motions of a Flexible Floating Barrier," *Journal of Hydronautics*, Vol. 5, 1971, pp. 41-51.

[2] Cross, R. H. and Hoult, D. P., "Oil Booms in Tidal Currents," *Proceedings of 12th Coastal Engineering Conference*, American Society of Civil Engineers, 1970, pp. 1745-1758.

[3] Wicks, M., "Fluid Dynamics of Floating Oil Containment by Mechanical Barriers in the Presence of Water Currents," *Proceedings of Joint Conference on Prevention and Control of Oil Spills*, American Petroleum Institute, 1969, pp. 55-106.

[4] Lindenmuth, W. T., Miller, E. R., and Hsu, C. C., "Studies of Oil Retention Boom Hydrodynamics," U.S. Government, Dept. of Transportation Report No. 714102/A/008, Dec. 1970.

[5] Von Karman, T., "The Engineer Grapples with Nonlinear Problems," *Bulletin of the American Mathematical Society*, Vol. 46, Aug. 1940, pp. 615-680.

[6] Benjamin, T. B., "Gravity Currents and Related Phenomena," *Journal of Fluid Mechanics*, Vol. 31, Pt. 2, 1968, pp. 209-248.

[7] Wilkinson, D. L., "Dynamics of Contained Oil Slicks," *Journal of the Hydraulics Division, Proceedings of the American Society of Civil Engineers*, Vol. 98, June 1972, pp. 1013-1030.

[8] Hale, L. A., Norton, D. J., and Rodenberger, C. A., "The Effects of Currents and Waves on an Oil Slick Retained by a Barrier," U.S. Government, Dept. of Transportation Report No. CG-D-53-75, 1974.

[9] Leibovich, S., "Oil Slick Instability and the Entrainment Failure of Oil Containment Booms," *Journal of Fluids Engineering*, Vol. 98, March 1976, pp. 98-105.

[10] Drazin, P. G., "Kelvin-Helmholtz Instability of Finite Amplitude," *Journal of Fluid Mechanics*, Vol. 42, Pt. 2, 1970, pp. 321-335.

[11] Van Houten, R. J., "Hydrodynamics of Contained Oil Slicks," Ph.D. Thesis, Dept. of Ocean Engineering, Massachusetts Institute of Technology, 1976.

[12] Milgram, J. H. and Van Houten, R. J., "A Flume for the Study of Contained Oil Slicks," Massachusetts Institute of Technology, Sea Grant Program Report MITSG 77-19, 1977.

[13] McCutchen, C. W., "Surface Films Compacted by Moving Water: Demarcation Lines Reveal Film Edges," *Science*, Vol. 170, Oct. 2, 1970, pp. 61-64.

[14] McDowell, R. S. and McCutchen, C. W., "The Thoreau-Reynolds Ridge, A Lost and Found Phenomenon," *Science*, Vol. 172, May 1971, pp. 971-973.

[15] Lamb, H., *Hydrodynamics*, Cambridge University Press, 1932, Art. 267-268.